



The Lyman Continuum Escape Survey. II. Ionizing Radiation as a Function of the [O III]/[O II] Line Ratio

Kimihiro Nakajima^{1,2}, Richard S. Ellis³, Brant E. Robertson⁴, Mengtao Tang⁵, and Daniel P. Stark⁵

¹Niels Bohr Institute, University of Copenhagen, Lyngbyvej 2, DK-2100 Copenhagen Ø, Denmark; knakajima@nbi.ku.dk

²Cosmic Dawn Center (DAWN), Denmark

³Department of Physics and Astronomy, University College London, Gower Street, London WC1E 6BT, UK

⁴Department of Astronomy & Astrophysics, University of California, Santa Cruz, 1156 High St., Santa Cruz, CA 95064, USA

⁵Steward Observatory, University of Arizona, 933 N. Cherry Ave., Tucson, AZ 85721, USA

Received 2019 September 15; revised 2019 December 25; accepted 2019 December 28; published 2020 February 4

Abstract

We discuss the rest-frame optical emission line spectra of a large (~ 50) sample of $z \sim 3.1$ Ly α emitting galaxies (LAEs) whose physical properties suggest such sources are promising analogs of galaxies in the reionization era. Reliable Lyman continuum (LyC) escape fractions have now been determined for a large sample of such LAEs from the LymAn Continuum Escape Survey (LACES) undertaken via deep *Hubble Space Telescope* imaging in the SSA22 survey area reported in Fletcher et al. Using new measures of [O II] emission secured from Keck MOSFIRE spectra we re-examine, for a larger sample, earlier claims that LyC leakages may correlate with the nebular emission line ratio [O III]/[O II] as expected for density-bound H II regions. We find that a large [O III]/[O II] line ratio is indeed a necessary condition for LyC leakage, strengthening earlier claims made using smaller samples at various redshifts. However, not all LAEs with large [O III]/[O II] line ratios are leakers and leaking radiation appears not to be associated with differences in other spectral diagnostics. This suggests the detection of leaking radiation is modulated by an additional property, possibly the viewing angle for porous H II regions. We discuss our new results in the context of the striking bimodality of LAE leakers and non-leakers found in the LACES program and the implications for the sources of cosmic reionization.

Unified Astronomy Thesaurus concepts: [High-redshift galaxies \(734\)](#); [Reionization \(1383\)](#); [Galaxy evolution \(594\)](#)

1. Introduction

The physical conditions that permit the leakage of ionizing radiation from star-forming galaxies is a topic of great interest. Recent analyses of the demographics and stellar properties of galaxies in the reionization era beyond a redshift $z \simeq 6$ suggest a fraction of 10%–20% of Lyman continuum (LyC) photons must escape a typical low-mass galaxy if such sources govern the process of cosmic reionization (Robertson et al. 2013; Bouwens et al. 2015; Stark 2016; Dayal & Ferrara 2018). Since direct measures of LyC leakage are not possible at high redshift due to foreground intergalactic medium (IGM) absorption, most recent work has focused on measures of the LyC escape fraction in low-redshift analogs (e.g., Siana et al. 2015; Vanzella et al. 2015; Shapley et al. 2016; Marchi et al. 2017; Rutkowski et al. 2017; Naidu et al. 2018; Steidel et al. 2018; Fletcher et al. 2019).

Ly α emitting galaxies (LAEs) are thought to be the most promising low-redshift analogs of sources in the reionization era on account of their low gas-phase metallicity and high star-formation rate. Ground-based spectroscopy reveals that many have intense [O III] emission (Nakajima et al. 2016; Trainor et al. 2016), a property which is inferred indirectly from *Spitzer* photometry for sources at $z > 6$ (Smit et al. 2015; Roberts-Borsani et al. 2016). The LymAn Continuum Escape Survey (LACES) was designed to image a sample of 61 $z = 3.1$ LAEs found using narrowband Subaru imaging in the SSA22 field (Hayashino et al. 2004; Matsuda et al. 2005; Yamada et al. 2012) using a broad-band F336W filter with the Wide Field Camera 3 onboard *Hubble Space Telescope* (*HST*; GO 14747, PI: Robertson). In our first paper in this series (Fletcher et al. 2019, hereafter Paper I), on the basis of spectral energy distribution (SED) fitting, we presented convincing evidence

for large escape fractions ($f_{\text{esc}} \sim 15\%–60\%$) for individual LAEs for 20% of the sample, in contrast to strict upper limits for the remainder. We found no strong correlation between this diversity of LyC radiation and other source properties such as stellar mass, UV luminosity, and the equivalent widths (EWs) of [O III] and Ly α . We speculated on the origin of this curious bimodality in the emergence of ionizing radiation.

The inter-dependence of f_{esc} and nebular line emission was discussed by Nakajima & Ouchi (2014) in terms of their photoionization models (see also Jaskot & Oey 2013). They found a possible correlation using the emission line ratio [O III]/[O II] (hereafter O32) which was interpreted in terms of “density-bound” H II regions. In contrast with “ionization-bound” H II regions where LyC photons are fully absorbed within the radius of the Stromgren sphere, unusually high values of O32 would reflect partially incomplete H II regions where some LyC photons could escape. In this respect, therefore, LAEs would be powerful sources capable of driving cosmic reionization (see also Marchi et al. 2018). At the time of submission of Paper I, a high fraction of the 61 LACES sources had coverage of [O III] emission from several Keck MOSFIRE campaigns (Nakajima et al. 2016) but the coverage of [O II] was limited. Accordingly, we have secured new MOSFIRE data improving the coverage of [O II] emission across the LACES sample so we can test for the expected trend between O32 and f_{esc} predicted by Nakajima & Ouchi (2014).

A plan of the paper follows. In Section 2 we discuss the new spectroscopic data, its reduction and estimates of [O II] emission and hence the O32 ratio. In Section 3 we revisit the LACES correlations in the context of our new line ratios as well as the strength of the ionizing radiation field. We discuss the results in the context of the bimodality of LyC leakage

Table 1
MOSFIRE Near-infrared Spectroscopy of the LACES Sample

Name	Band	Date	Seeing	Exp. (hr)	N^a (1)	References (2)
mask1	<i>K</i>	2015 Jun 20	0''4–0''5	3.0	17	(a)
	<i>H</i>	2015 Jun 21	0''4–0''5	2.5	17	(a)
mask2	<i>K</i>	2017 Jul 31	0''6–0''9	3.0	21	(b)
	<i>H</i>	2017 Aug 1	0''5–0''9	3.1	21	(b)
mask3	<i>K</i>	2017 Aug 1	0''5–0''8	2.3	17	(b)
mask4	<i>K</i>	2017 Aug 1	0''3–0''5	2.0	19	(b)
mask5	<i>H</i>	2018 Aug 3, 4	0''4–0''8	4.6	21	(c)
	Full ^a	<i>K</i>		2.0–6.0	53	(c)
	<i>H</i>			2.5–10.2	38	(c)

Note. (1) Number of targeted LACES sources. (2) Relevant campaigns (a) Nakajima et al. (2016); (b) Paper I; (c) This work.

^a Full sample in *K* and *H* taking into account multiply observed spectra.

found in Paper I in Section 4. Throughout the paper we adopt a concordance cosmology with $\Omega_\Lambda = 0.7$, $\Omega_M = 0.3$, and $H_0 = 70 \text{ km s}^{-1} \text{ Mpc}^{-1}$.

2. Data

2.1. MOSFIRE Observations and Data Reduction

Early MOSFIRE observations undertaken in the LACES area were described in Nakajima et al. (2016) and Paper I. As a pilot observation, Nakajima et al. (2016) discuss data for one MOSFIRE pointing (referred to here as mask 1), spectroscopically covered in the *K*-band (sampling [O III] and $H\beta$) and the *H*-band (sampling [O II] and [Ne III]). *HST*/F336W coverage of LACES was determined in part based on this pilot observation. In Paper I, additional *K*-band spectroscopy for three further MOSFIRE pointings was presented (masks 2–4), one of which (mask 2) was also sampled in the *H*-band. These additional pointings were chosen to include as many LACES sources as possible with minimal overlap with mask 1. Mask 4 covered almost the same area as mask 2, and was designed primarily to increase the depth for those sources whose *K*-band spectra were of low signal/noise.

In this paper we present MOSFIRE data from a further pointing (mask 5) undertaken via a long integration in the *H*-band with the specific goal of improving the coverage of [O II] emission for sources well-studied in the *K*-band (i.e., [O III]) in masks 2–4. The new *H*-band observations were taken in two second-half nights on UT 2018 August 3 and 4 in clear conditions with a seeing of 0''4–0''8. Observations were conducted in a similar manner to those reported earlier, adopting a slit width of 0''7 and individual exposure times of 120 s with an AB nod sequence of 3'' separation. The total integration time for mask 5 was 4.6 hr. Table 1 provides a summary of our near-infrared spectroscopic campaign of the LACES sample.

Data reduction was performed using the MOSFIRE DRP⁶ in the manner described in Nakajima et al. (2016). All spectroscopic data listed in Table 1 were re-reduced with the latest (2018) version of MOSFIRE DRP. Briefly, the processing includes flat-fielding, wavelength calibration, background

subtraction, and combining the nod positions. Wavelength calibration in the *H*-band was performed using OH sky lines and in the *K*-band via a combination of OH lines and Neon arcs. Flux calibration and telluric absorption corrections were obtained from A0V *Hipparcos* stars observed on the same night under the same seeing conditions, at similar air masses adopting the same slit width. This procedure corrects for slit losses since most of our LAEs were confirmed with *HST* images to be unresolved in our ground-based conditions. The cross-calibration between the *H*- and *K*-band was independently checked and confirmed with bright stars ($K_{\text{Vega}} = 15.5\text{--}16.5$) included on each mask. Some Lyman-break galaxies (LBGs) that were also placed on the masks for a comparison sample are more extended than LAEs in the *HST* image, and their slit losses would not be fully corrected for with the above method. We quantified the potential additional slit losses for the LBGs by using an appropriately smoothed *HST* image using the seeing and slit position/angles appropriate for the observations. We find for the small subset of LBG targets, the additional flux losses would be smaller than 25%. This is minimal and does not affect our conclusions.

The resulting *K*-band observations span four different masks, including 18 objects that were observed on more than one mask. For each of these multiply observed sources, we combined flux-calibrated 2D spectra from different masks to generate a final 2D spectrum after the spatial zero-points were aligned. Our final *K*-band spectroscopic sample contains 53 LACES sources each with a total integration time ranging from 2.0 to 6.0 hr. Similarly, we have *H*-band coverage of 38 LACES sources with integration times ranging from 2.5 to 10.2 hr. All *H*-band sources have *K*-band coverage. We experimented with coaddition of the various integrations using both 2D spectra from which 1D spectra were subsequently extracted, as well as summation of 1D spectra individually extracted; no significant difference in signal-to-noise ratio (S/N) was found.

1D spectra were produced via the summation of 5–9 pixels along the spatial direction centered on the expected spatial position. This width was chosen to maximize the S/N and corresponds approximately to twice the average seeing for the observations.

2.2. Emission Line Identifications

Out of the 53 *K*-band sources, 38 have confirmed Ly α emission from our earlier optical campaigns (see Nakajima et al. 2018a for details). For the other LAEs, their redshifts are fairly well-constrained from the Subaru narrowband filter used for the selection. Using these redshifts as an initial guess, we visually examined the 1D and 2D spectra for detectable [O III] $\lambda\lambda 5007, 4959$ and $H\beta$ emission. One or both of [O III] and $H\beta$ were detected in the MOSFIRE *K*-band data for 43 of the 53 *K*-band sources and their line fluxes were measured. We then proceeded to measure fluxes for the [O II] doublet⁷ and [Ne III] emission in the cases where *H*-band spectra are available (31 out of the 43 with line emission in the *K*-band). All *H*-band line fluxes were measured by fitting a Gaussian profile using the IRAF task SPECFIT adopting the redshift and FWHM of the [O III] $\lambda 5007$. A constant continuum was also considered for

⁶ <https://keck-datareductionpipelines.github.io/MosfireDRP>

⁷ We use the notation [O II] $\lambda 3727$, or simply [O II], as the sum of the doublet. In the fitting process, we adopted two Gaussians unless otherwise noted.

Table 2
Optical Emission Line Fluxes

Obj.	[O II] Doublet	[Ne III] λ 3869	H β	[O III] λ 4959	[O III] λ 5007
M38	8.5 \pm 0.3	1.9 \pm 0.2	5.3 \pm 0.1	6.8 \pm 0.1	20.5 \pm 0.1
2132	7.6 \pm 0.5	1.4 \pm 0.2	2.8 \pm 0.3	5.9 \pm 0.3	15.3 \pm 0.3
104037 ^(a,S)	3.6 \pm 0.1	1.4 \pm 0.1	2.6 \pm 0.1	6.9 \pm 0.1	14.5 \pm 0.1
93564 ^(a,G)	1.8 \pm 0.2	0.4 \pm 0.1	2.1 \pm 0.2	5.2 \pm 0.3	13.2 \pm 0.3
104511	0.9 \pm 0.2	0.9 \pm 0.1	2.2 \pm 0.2	5.2 \pm 0.1	12.0 \pm 0.1
108679	<0.8	3.5 \pm 0.3	10.6 \pm 0.3
96688	4.1 \pm 0.3	1.7 \pm 0.2	1.1 \pm 0.2	3.1 \pm 0.2	10.0 \pm 0.2
99330	1.0 \pm 0.1	0.5 \pm 0.1	1.1 \pm 0.1	2.6 \pm 0.1	8.0 \pm 0.1
109140	<0.9	2.1 \pm 0.2	5.8 \pm 0.2
86861 ^{(a,G)b}	<0.7	0.9 \pm 0.2	0.7 \pm 0.0	1.7 \pm 0.2	5.4 \pm 0.2
97030	0.9 \pm 0.2	0.4 \pm 0.1	0.7 \pm 0.1	1.7 \pm 0.1	4.7 \pm 0.1
92017	<0.8	0.8 \pm 0.2	4.0 \pm 0.2
106500	<0.5	0.5 \pm 0.1	1.2 \pm 0.1	1.2 \pm 0.2	3.5 \pm 0.2
104097	1.8 \pm 0.1	<0.3	1.2 \pm 0.1	1.0 \pm 0.1	3.1 \pm 0.1
102334	0.7 \pm 0.2	1.0 \pm 0.2	2.9 \pm 0.2
94460 ^(a,S)	<0.2	<0.2	0.4 \pm 0.1	0.9 \pm 0.1	2.8 \pm 0.1
102826	2.0 \pm 0.1	<0.3	0.7 \pm 0.1	<0.3	2.8 \pm 0.1
107585	<0.4	<0.6	1.0 \pm 0.2	0.8 \pm 0.2	2.3 \pm 0.2
110896	<0.7	<0.7	2.3 \pm 0.2
89114	<0.4	<0.4	<0.3	0.8 \pm 0.1	2.3 \pm 0.1
99415	<0.4	<0.3	0.5 \pm 0.1	0.5 \pm 0.1	1.9 \pm 0.1
97081	<0.2	<0.2	0.3 \pm 0.1	0.6 \pm 0.1	1.9 \pm 0.1
90428	<0.4	<1.0	1.7 \pm 0.3
93474	<0.3	<0.4	<0.5	0.6 \pm 0.1	1.7 \pm 0.1
85165	<1.0	<1.6	0.8 \pm 0.2	0.8 \pm 0.2	1.6 \pm 0.2
92616 ^(a,G)	<0.3	<0.4	1.5 \pm 0.1
104147	<0.2	0.2 \pm 0.1	<0.2	0.2 \pm 0.1	1.4 \pm 0.1
92219	<0.3	<0.3	<0.3	<0.2	1.4 \pm 0.1
93004	<0.4	0.7 \pm 0.1	1.4 \pm 0.1
92235	0.5 \pm 0.1	<0.3	0.4 \pm 0.1	<0.4	1.4 \pm 0.1
97254	<0.2	<0.2	0.3 \pm 0.1	0.8 \pm 0.1	1.3 \pm 0.1
97176	0.3 \pm 0.1	0.3 \pm 0.1	<0.2	0.4 \pm 0.1	1.3 \pm 0.1
103371	<0.2	<0.2	0.2 \pm 0.1	0.9 \pm 0.1	1.3 \pm 0.1
89723	<0.2	<0.2	<0.2	0.5 \pm 0.1	1.3 \pm 0.1
110290	<0.3	<0.3	0.4 \pm 0.1	<0.6	1.1 \pm 0.2
93981	0.4 \pm 0.1	0.4 \pm 0.1	1.1 \pm 0.1
105937 ^(a,S)	<0.4	<0.3	<0.9	0.4 \pm 0.1	1.0 \pm 0.1
91055	<0.3	<0.2	0.3 \pm 0.1	0.3 \pm 0.1	0.9 \pm 0.1
107677	<1.0	<0.5	0.9 \pm 0.2
95217	<0.4	<0.2	<0.6	<0.4	0.8 \pm 0.1
97128	0.7 \pm 0.2	<0.5	0.7 \pm 0.2
101846 ^(a,S)	<0.3	<0.3	<0.3	<0.3	0.4 \pm 0.1
90675 ^{(a,G)c}	2.0 \pm 0.2	<0.5	<0.5

Notes. Fluxes and their 1σ errors are given in units of 10^{-17} erg s $^{-1}$ cm $^{-2}$. Upper limits represent the 3σ values.

^a LyC leaking candidates from Paper I. The *G* and *S* denotes the Gold and Silver sample, respectively.

^b The single LAE-AGN in the LACES sample.

^c This LAE is likely an extremely metal-poor galaxy on account of its low [O III]/H β , large H β and Ly α EWs, and high ξ_{ion} (see also Table 4).

each of the [O III]+H β and [O II]+[Ne III] lines in accounting for background residuals.

To estimate the sky noise level and hence the flux uncertainties, we used more than 1000 apertures with a size equal to that adopted for the flux measurements spread randomly around the emission lines in the 2D spectrum after masking pixels heavily contaminated by OH lines. We then derived the 1σ fluctuation for each of the lines according to the distribution of the photon counts measured with the randomly distributed apertures. Table 2 lists the measured fluxes and their 1σ errors for the 43 identified objects. Among these identified sources, there are 26, 12, and 12 objects whose H β , [O II], and [Ne III] can be individually detected, respectively.

For the 10 remaining sources with MOSFIRE spectra, three have a spectroscopic redshift based on Ly α , where [O III] λ 5007 cannot reliably be detected due to a strong OH line.⁸ For the other 7 targets, without a redshift we cannot determine the expected wavelength of [O III] λ 5007 or any other lines and hence upper limits on their fluxes. We therefore exclude these 10 sources in the following discussion.

Paper I presented 12 individual LAEs with prominent escape fractions; $f_{\text{esc}} \sim 15\% - 60\%$. Out of these 12 f_{esc} -detected

⁸ This assumes the velocity offset of Ly α is smaller than ~ 200 km s $^{-1}$ corresponding to twice the resolution of MOSFIRE in the *K*-band as is typical for LAEs (e.g., Nakajima et al. 2018a).

Table 3
Subsamples of the LACES MOSFIRE Campaign

Subsample	for Line Ratios	for EWs in K/H	for ξ_{ion}
LyC-LAEs ^a	5	5/5	6
noLyC-LAEs	20	24/17	29
LBGs	5	5/5	6

Note.

^a A single AGN-LAE, AGN86861, whose LyC radiation was identified in Paper I has been removed for the stacking analysis and is not counted here.

sources,⁹ 11 (9) have $K + H$ (only K) band MOSFIRE spectra, from which 8 present one or more rest-frame optical emission lines as listed in Table 2. These 8 sources also have Ly α detections. The remaining 4 prominent leakers have neither Ly α nor rest-frame optical emission lines; that is they lie in the subsample of 10 sources discussed above and will not be considered further in this paper.

2.3. Stacked Spectra

Despite our significant integration times, we only directly detect individual [O III] emission lines in a subset of our data (Section 2.2, Table 2). To exploit the full diagnostic value of the rest-frame optical emission lines, we therefore developed a stacking procedure for various subsamples of the LACES catalog. Our goal is to use the stacked spectra to derive average line strengths, line ratios, and measures of the ionizing radiation field ξ_{ion} (see Section 3.2 for definition and more details) and to correlate these properties with the strength of LyC leakage as determined in Paper I.

Accordingly, we divided our spectroscopic sample into three subsamples: LAEs with a clear LyC detection defined as a $>4\sigma$ detection in Paper I (hereafter called “LyC-LAEs” subsample), those LAEs without a clear LyC signal (“noLyC-LAEs” subsample), and LBGs, none of which reveal a LyC signal (“LBGs” subsample). To distinguish LAEs from LBGs we adopted a rest-frame EW of 20 Å, derived spectroscopically and/or photometrically, as the demarcation level. The LyC-LAEs subsample includes both the Gold and Silver subsamples in Paper I but excludes the non-thermal source AGN 86861. The numbers of sources in each of the subsamples are given in Table 3.

It is important to note that the individual spectra must be normalized in a different manner prior to stacking depending on the physical quantity we seek to measure. For individual line ratios, we use the [O III] line flux, whereas for EWs and the ξ_{ion} parameter we use the rest-frame optical and UV continuum, respectively, derived from the *HST*/F160W and the Subaru optical photometry. Naturally for line ratios, we require both H - and K -band spectra, whereas for individual measures of $H\beta$ or [O III] only K -band data is required. Thus, the numbers of useful spectra for stacking varies according to the physical quantity concerned. The details are given in Table 3.

We adopted a stacking procedure very similar to that described in Nakajima et al. (2018a). Briefly, using the individual flux-calibrated spectra in K (H), we shifted each to its rest-frame and rebinned the spectrum to a common dispersion of 0.55 (0.40) Å per pixel. The spectra were then

median-stacked with the appropriate normalization as explained above. To exclude positive and negative sky subtraction residuals, we rejected an equal number of the highest and lowest outliers at each pixel corresponding in total to $\simeq 5\%$ of the data. Using an averaging method led to spectra almost indistinguishable from using the median.

To evaluate sample variance and statistical noise, we adopted a bootstrap technique similar to that described in Nakajima et al. (2018a). We generated 1000 fake composite spectra from the chosen sample. Each fake spectrum was constructed in the same way, using the same number of spectra as the actual composite, but with the list of input spectra formulated by selecting spectra at random, with replacement, from the full list. With these 1000 fake spectra, we derived the standard deviation at each spectral pixel. The standard deviations are taken into account in calculating the uncertainties of each line flux.

The composite spectra for the three subsamples normalized by their [O III] fluxes are shown in Figure 1. It is evident that all the key diagnostic emission lines are significantly identified. The difference between the stacked spectra of LAEs and LBGs is immediately apparent e.g., in the [O III]/[O II] and [Ne III]/[O II] line ratios. The various properties derived from the individual and composite spectra are listed in Table 4.

2.4. Dust Correction to the Nebular Spectra

Prior to quantitative analysis, it is necessary to consider corrections for dust reddening, particularly for line flux ratios and the ξ_{ion} parameter. Since multiple Balmer emission lines cannot be reliably identified in the individual spectra, the amount of reddening must be estimated using the stellar continuum, assuming that nebular emission and the stellar continuum suffer similar attenuation. Although this assumption remains open to debate at high- z , it appears reasonable for young, low-mass star-forming galaxies appropriate for our sample (SFR $\sim 1\text{--}10M_{\odot}\text{ yr}^{-1}$ and $M_{\star} \sim 10^{8.5}\text{--}10^{9.5}M_{\odot}$; e.g., Reddy et al. 2015).

Earlier studies have tended to indicate LAEs are largely dust-free systems (e.g., Erb et al. 2016; Trainor et al. 2016). Using the SMC extinction curve (Gordon et al. 2003) and the Binary Population and Spectral Synthesis SEDs, Paper I conducted SED model fitting to constrain the stellar population parameters as well as the amount of dust attenuating the stellar continuum emission. That analysis returned an almost negligible dust attenuation for LAEs irrespective of LyC identification with $E(B - V) \simeq 0.01$. Such a small amount of dust is also discussed and supported by our pilot observations in Nakajima et al. (2016), where small Balmer decrements for two bright LAEs were shown to be consistent with zero reddening. Furthermore, Tang et al. (2019) illustrate a monotonic decrease of nebular attenuation with increasing EW of [O III], showing that the most extreme line emitters with $\text{EW}([\text{O III}]) \gtrsim 800\text{ \AA}$ have almost no dust attenuation effect on the nebular emission lines. The relationship derived in Tang et al. (2019) supports the assumption of little dust correction for the LAE sample, given their extremely strong [O III] emission in general (Section 3). A similar implication is also drawn in Erb et al. (2016) using the O32 line ratio. A larger value of $E(B - V) \simeq 0.10$ was inferred on average for the LBG subsample following the same SED fitting procedure.

Because the $E(B - V)$ value is generally uncertain for individual faint sources, we adopt the average of $E(B - V) = 0.01$ for all the individual and composite spectra for the LAE subsamples, and

⁹ This subsample includes both the Gold and Silver classifications of Paper I.

Table 4
Physical Properties of the MOSFIRE-identified Sources and their Composites

Obj.	M_{UV}	EW(Ly α) (Å)	z_{sys}	$\Delta v_{Ly\alpha}$ (km s $^{-1}$)	EW([O III]) (Å)	EW(H β) (Å)	[O III]/H β	R23	O32	log ξ_{ion} (Hz erg $^{-1}$)	f_{esc}
M38	-21.5 ± 0.0	...	3.2911	...	487.1 ± 4.8	93.9 ± 2.4	5.1 ± 0.1	7.0 ± 0.2	2.8 ± 0.1	25.42 ± 0.02	...
2132	-21.9 ± 0.0	7 $^{+2}_{-2}$	3.0586	...	384.3 ± 7.8	51.0 ± 4.7	7.5 ± 0.7	10.5 ± 1.0	2.4 ± 0.2	24.91 ± 0.04	...
104037 ^(a,S)	-21.3 ± 0.0	36 $^{+3}_{-2}$	3.0650	224.2	791.3 ± 17.4	96.3 ± 4.4	8.2 ± 0.3	9.6 ± 0.4	5.9 ± 0.2	25.52 ± 0.02	0.13 ± 0.02
93564 ^(a,G)	-21.2 ± 0.0	59 $^{+6}_{-6}$	3.6770	545.5	1040.5 ± 33.7	120.7 ± 11.6	8.6 ± 0.8	9.5 ± 0.9	10.0 ± 0.9	25.72 ± 0.05	0.31 ± 0.03
104511	-20.6 ± 0.1	26 $^{+4}_{-4}$	3.0645	...	1351.7 ± 44.7	173.8 ± 14.2	7.8 ± 0.6	8.2 ± 0.6	19.7 ± 3.7	25.70 ± 0.04	...
108679	-19.8 ± 0.1	54 $^{+11}_{-10}$	3.1066	335.1	1598.8 ± 87.2	<96.1	>16.6	<25.60	...
96688	-21.9 ± 0.0	-1 $^{+1}_{-1}$	3.1107	...	247.0 ± 5.0	21.4 ± 4.4	11.4 ± 2.4	15.5 ± 3.2	2.8 ± 0.2	24.54 ± 0.08	...
99330	-19.9 ± 0.1	52 $^{+7}_{-6}$	3.1057	341.7	1696.7 ± 116.5	169.5 ± 18.7	10.0 ± 0.7	11.0 ± 0.8	10.2 ± 1.2	25.65 ± 0.05	...
109140	-19.5 ± 0.2	65 $^{+18}_{-15}$	3.1090	...	2428.9 ± 262.3	<268.7	>9.0	<25.75	...
86861 ^{(a,G)b}	-21.4 ± 0.0	81 $^{+3}_{-3}$	3.1054	217.6	295.4 ± 13.3	30.3 ± 1.6	9.7 ± 0.7	9.7 ± 0.7	>10.0	25.18 ± 0.05	0.46 ± 0.05
97030	-19.2 ± 0.2	26 $^{+11}_{-9}$	3.0735	...	853.7 ± 82.5	91.0 ± 14.5	9.4 ± 1.0	10.8 ± 1.1	6.6 ± 1.1	25.72 ± 0.09	...
92017	-19.0 ± 0.3	>90	3.1070	143.8	>6.0	<25.89	...
106500	-19.1 ± 0.2	90 $^{+40}_{-30}$	3.0581	...	2201.7 ± 437.2	559.8 ± 150.5	3.9 ± 0.5	3.9 ± 0.5	>9.5	26.00 ± 0.10	...
104097	-20.8 ± 0.1	-1 $^{+8}_{-8}$	3.0674	...	173.1 ± 7.1	48.9 ± 2.7	3.5 ± 0.2	5.3 ± 0.3	2.0 ± 0.2	25.00 ± 0.03	...
102334	-20.2 ± 0.1	30 $^{+5}_{-4}$	3.0902	203.0	301.8 ± 21.0	54.6 ± 12.5	5.5 ± 1.3	25.34 ± 0.09	...
94460 ^(a,S)	-19.9 ± 0.1	51 $^{+9}_{-8}$	3.0723	157.5	384.9 ± 21.6	45.8 ± 11.6	8.4 ± 2.1	8.4 ± 2.1	>17.3	25.45 ± 0.11	0.33 ± 0.02
102826	-21.1 ± 0.0	-4 $^{+4}_{-3}$	3.0714	...	94.4 ± 4.4	17.0 ± 3.0	5.5 ± 1.0	9.0 ± 1.6	1.6 ± 0.1	24.62 ± 0.07	...
107585	-19.3 ± 0.2	25 $^{+11}_{-8}$	3.0895	3.1 ± 0.8	3.1 ± 0.8	>7.8	25.85 ± 0.11	...
110896	-20.7 ± 0.1	9 $^{+2}_{-2}$	3.0644	>4.3	<24.79	...
89114	-19.5 ± 0.2	40 $^{+10}_{-9}$	3.0832	...	1219.7 ± 104.9	<135.5	>9.0	>9.0	>8.6	<25.33	...
99415	-19.2 ± 0.2	62 $^{+21}_{-16}$	3.0972	...	1019.7 ± 233.8	193.9 ± 62.9	5.3 ± 1.0	5.3 ± 1.0	>6.6	25.59 ± 0.11	...
97081	>-18.7	>208	3.0762	178.0	>1890.0	>197.2	9.6 ± 2.7	9.6 ± 2.7	>10.4	>25.52	...
90428	-19.4 ± 0.2	51 $^{+10}_{-8}$	3.1037	230.1	>1743.6	...	>5.2	<25.46	...
93474	-19.3 ± 0.2	50 $^{+16}_{-13}$	3.0702	363.1	2056.9 ± 383.3	<428.3	>4.8	>4.8	>7.0	<25.55	...
85165	-21.5 ± 0.0	35 $^{+2}_{-2}$	3.0996	...	56.8 ± 8.3	18.3 ± 4.8	3.1 ± 0.9	3.1 ± 0.9	>2.3	24.88 ± 0.10	...
92616 ^(a,G)	-19.5 ± 0.2	49 $^{+13}_{-11}$	3.0714	253.3	>6.2	<25.68	0.60 ± 0.09
104147	-19.4 ± 0.2	24 $^{+8}_{-6}$	3.0994	389.8	371.6 ± 60.2	<35.2	>10.5	>10.5	>7.9
92219	-19.5 ± 0.2	115 $^{+22}_{-18}$	3.1008	182.8	>7.4	>7.4	>5.7
93004	-19.4 ± 0.2	38 $^{+13}_{-11}$	3.1127	212.8	1050.6 ± 170.9	<221.3	>4.7	<25.49	...
92235	-20.2 ± 0.1	29 $^{+6}_{-5}$	3.0713	...	189.9 ± 17.7	42.3 ± 12.2	4.5 ± 1.3	5.8 ± 1.7	3.5 ± 0.6	25.13 ± 0.11	...
97254	-18.9 ± 0.3	68 $^{+24}_{-19}$	3.0712	251.8	745.1 ± 94.3	109.0 ± 29.1	6.8 ± 1.5	6.8 ± 1.5	>9.6	25.49 ± 0.13	...
97176	-19.8 ± 0.1	60 $^{+15}_{-12}$	3.0751	219.2	288.9 ± 27.7	<40.7	>7.1	>8.5	5.1 ± 1.2	<25.10	...
103371	>-18.7	151 $^{+72}_{-46}$	3.0894	-20.5	>1665.5	>174.0	9.6 ± 2.8	9.6 ± 2.8	>9.9	>25.47	...
89723	-20.5 ± 0.1	99 $^{+26}_{-20}$	3.1113	259.6	>9.1	>9.1	>8.8
110290	-19.3 ± 0.2	56 $^{+20}_{-15}$	3.1088	103.6	653.8 ± 170.4	198.8 ± 71.7	3.3 ± 1.1	3.3 ± 1.1	>4.5	25.53 ± 0.13	...
93981	>-18.7	>71	3.0766	...	731.1 ± 94.6	220.5 ± 51.8	3.3 ± 0.7	>25.74	...
105937 ^(a,S)	-20.2 ± 0.1	31 $^{+8}_{-7}$	3.0666	155.5	104.1 ± 15.4	<65.9	>1.6	>1.6	>3.4	<25.62	0.32 ± 0.07
91055	>-18.7	>76	3.0818	254.9	1041.0 ± 173.1	218.9 ± 80.1	4.8 ± 1.5	4.8 ± 1.5	>4.6	>25.53	...
107677	>-18.7	>109	3.0679	47.2	>1.2
95217	-19.0 ± 0.3	81 $^{+49}_{-32}$	3.0668	...	1020.4 ± 372.0	<526.3	>1.9	>1.9	>2.8	<25.73	...
97128	>-18.7	>81	3.0725	...	>751.8	>552.5	1.4 ± 0.5	>25.96	...
101846 ^(a,S)	>-18.7	>147	3.0565	232.1	>166.6	...	>1.5	>1.5	>1.9	...	0.42 ± 0.09
90675 ^(a,G)	>-18.7	>61	3.1110	-3.6	<128.9	252.5 ± 32.7	<0.4	>26.41	0.39 ± 0.11

Table 4
(Continued)

Obj.	M_{UV}	EW(Ly α) (\AA)	z_{sys}	$\Delta v_{\text{Ly}\alpha}$ (km s^{-1})	EW([O III]) (\AA)	EW(H β) (\AA)	[O III]/H β	R23	O32	$\log \xi_{\text{ion}}$ (Hz erg^{-1})	f_{esc}
Composite Spectra											
LyC-LAEs	-20.1 ± 0.6	44 ± 11	$600.0^{+293.5}_{-206.8}$	$99.2^{+32.2}_{-31.1}$	$7.0^{+2.4}_{-2.4}$	$7.6^{+2.6}_{-2.6}$	$10.5^{+3.0}_{-3.0}$	$25.65^{+0.11}_{-0.18}$	0.35 ± 0.14
noLyC-LAEs	-19.4 ± 0.6	64 ± 27	$1067.0^{+182.0}_{-157.2}$	$126.8^{+43.3}_{-34.9}$	$7.7^{+1.7}_{-1.4}$	$8.4^{+1.9}_{-1.6}$	$12.7^{+7.5}_{-6.7}$	$25.50^{+0.09}_{-0.09}$	$<0.005^c$
LBGs	-21.3 ± 0.5	$0.5 \pm 4.$	$266.8^{+78.8}_{-31.9}$	$40.3^{+17.7}_{-15.1}$	$7.0^{+1.2}_{-0.9}$	$10.5^{+1.7}_{-1.7}$	$2.0^{+0.7}_{-0.5}$	$25.05^{+0.05}_{-0.08}$	$<0.005^c$

Notes. Upper/lower limits represent the 3σ values. For the EW measurements of [O III] and H β , we use the *HST*/F160W photometry in determining the continuum level (see Paper I). No constraint on EW is thus given if the object lacks the F160W coverage.

^a LyC leaking candidates from Paper I. The *G* and *S* denotes the Gold and Silver sample, respectively.

^b The single LAE-AGN in the LACES sample.

^c The upper-limit is drawn from the composite of all the non-detections including both LAEs and LBGs Paper I.

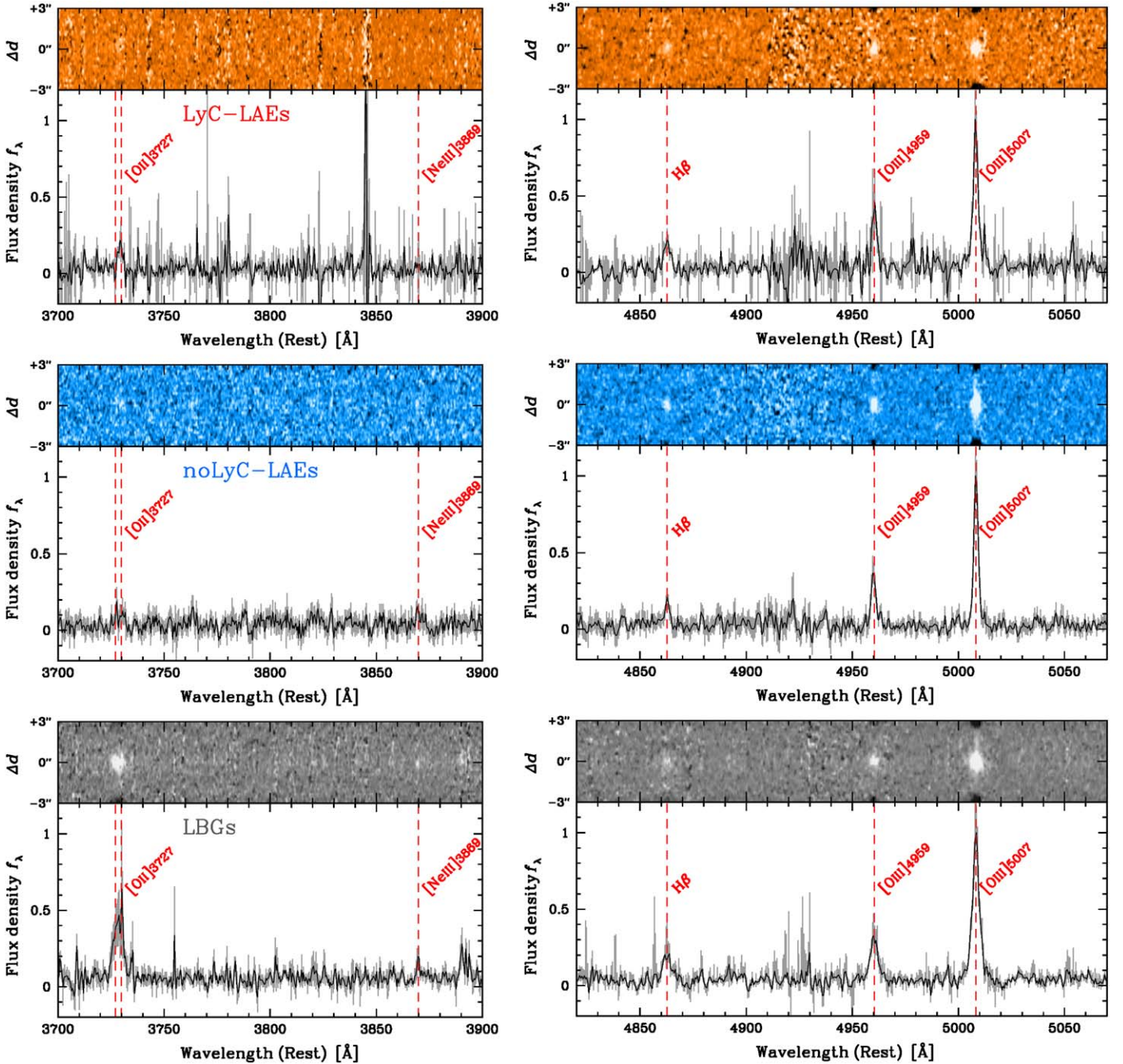


Figure 1. Composite rest-frame optical spectra of LAEs with a significant *HST* LyC detection (LyC-LAEs; top), LAEs with no detectable LyC flux (noLyC-LAEs; middle), and LBGs (all undetected in LyC; bottom). These spectra were generated with the [O III]-normalized individual spectra for measuring line flux ratios (see text for more details). The gray shaded region around each spectrum refers to the standard deviation of the flux density at each wavelength estimated by bootstrap resampling (see the text for details). The wavelengths of key diagnostic emission lines are marked with a red dashed line.

$E(B - V) = 0.10$ for the LBGs subsample in the following analysis.

3. Analysis

3.1. Emission Lines as a Function of f_{esc}

We now discuss the correlation between the LyC detections presented in Paper I and both the individual and stacked line measurements derived for the various subsamples of our MOSFIRE spectra. We begin with individual line measures

updating and extending some of the results presented in Paper I.

Figure 2 shows that LAEs on average present an intense [O III] emission line with a rest-frame EW of $\simeq 600\text{--}1100 \text{ \AA}$, consistent with the results of our pilot MOSFIRE program (Nakajima et al. 2016). Our enlarged spectroscopic data also reveals more intense $H\beta$ emission with an EW of $>100 \text{ \AA}$. A combined EW of [O III]+ $H\beta$ of $\simeq 700\text{--}1200 \text{ \AA}$ confirms the suggestion that such intermediate redshift LAEs are close analogs of galaxies in the reionization era where the similarly large EWs have been inferred from *Spitzer* photometry (e.g.,

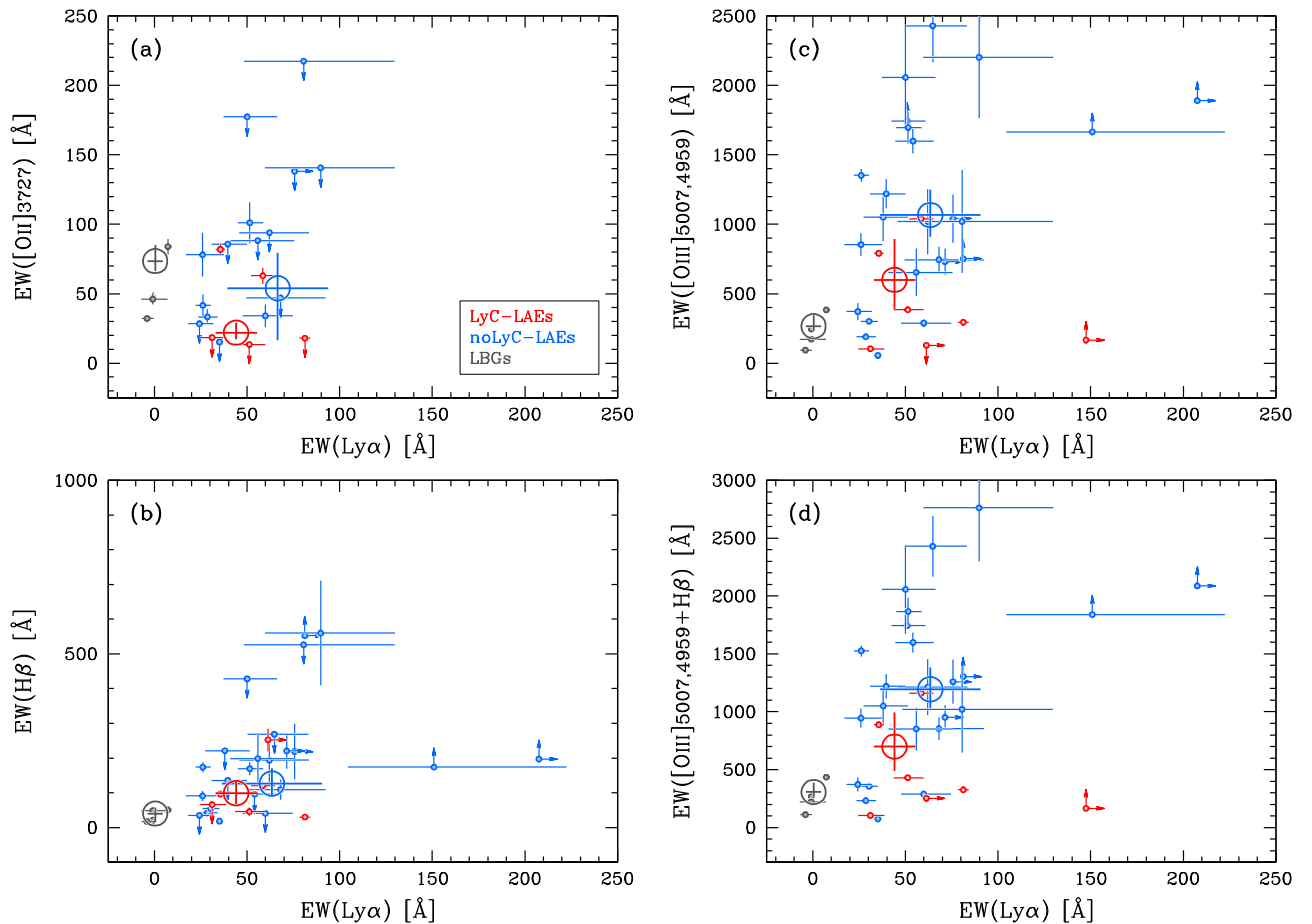


Figure 2. Rest-frame equivalent widths (EWs) of (a) [O II], (b) H β , (c) [O III], and (d) [O III]+H β for the three LACES subsamples (LyC-LAEs in red, noLyC-LAEs in blue, and LBGs in gray) as a function of EW(Ly α). Large symbols represent results from stacked spectra, whereas the small faint-colored circles shows individual measurements with 3σ upper limits shown as arrows.

Smit et al. 2015; Roberts-Borsani et al. 2016; see also Reddy et al. 2018; Tang et al. 2019).

One of the most interesting questions we can now consider is, via our various spectroscopic measures, what is the physical origin of the bimodal nature of LyC emission seen in the LACES sample (Paper I). In Paper I, we presented a preliminary EW([O III]) distribution that revealed no significant difference between those LAEs with and without a LyC detection. We can see this is also the case in Figure 2 and the conclusion would not be changed after correcting by a $(1 - f_{\text{esc}})$ factor in order to compensate for escaping (i.e., unconsumed) numbers of ionizing photons.

However, when we turn to consideration of the [O III]/[O II] ratio, which we could not consider in Paper I, a more interesting result emerges. This ratio represents the degree of ionization in the hot ISM and, using photoionization models, Nakajima & Ouchi (2014) argued that intense high ionization lines, e.g., [O III], and weaker low-ionization lines, e.g., [O II], could arise from density-bounded H II regions. The associated porosity of the star-forming regions to ionizing radiation would lead to a high f_{esc} (see also Jaskot & Oey 2013; Zackrisson et al. 2013; Behrens et al. 2014).

Figure 3 presents the relationship between f_{esc} and [O III]/[O II] line ratio for the LACES LyC-LAEs subsample. Our stacked LyC subsample with an average escape fraction $f_{\text{esc}} \sim 0.35$ has a large [O III]/[O II] line ratio of $\simeq 10$. Combining this measurement with individual LyC leaking

sources at low- z (Izotov et al. 2016a, 2016b, 2018a, 2018b) as well as a single $z = 3$ LyC emitter, *Ion2* (de Barros et al. 2016; Vanzella et al. 2016, 2020), strengthens the positive correlation presented by Izotov et al. (2018a) and Faisst (2016). Figure 3 shows that a large [O III]/[O II] ratio is a necessary condition for sources with a high f_{esc} . Significantly, the high escape fraction inferred ($f_{\text{esc}} > 0.1$) is approximately the lower limit necessary if star-forming galaxies govern the reionization process (e.g., Robertson et al. 2015). In our sample, these are only found if the [O III]/[O II] ratio exceeds ~ 6 –7.

On the other hand, a large [O III]/[O II] line ratio need not in every case imply a prominent LyC flux, as can be inferred also from the composite spectrum of the noLyC-LAEs (middle panel in Figure 1). This contradiction is also apparent in low-redshift green pea galaxies (Izotov et al. 2018b; Jaskot et al. 2019). We evaluate this further in Figure 4, where we compare our LAEs with and without a LyC detection in the [O III]/[O II] line ratio versus R23-index diagnostic diagram. This diagram is widely used to examine the gas-phase metallicity and ionization state in the local universe (e.g., Kewley & Dopita 2002) as well as at $z = 2$ –4 (e.g., Maiolino et al. 2008; Nakajima & Ouchi 2014; Shapley et al. 2015; Onodera et al. 2016; Strom et al. 2017; Sanders et al. 2020). A relatively large scatter in the R23-index at fixed [O III]/[O II] is seen, although for those sources the [O III]/[O II] measure is only a lower limit (Table 2). This may reflect a low metallicity tail to the distribution for which much larger [O III]/[O II] indices are

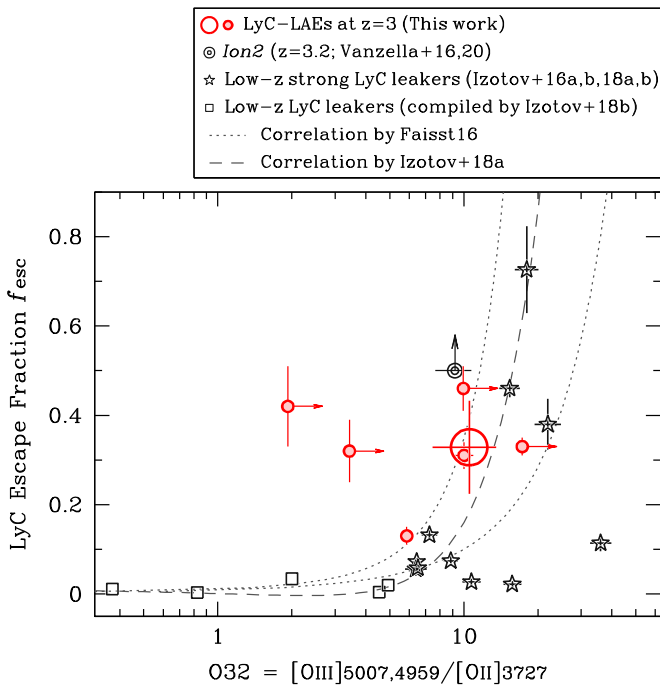


Figure 3. O32 line ratio vs. escape fraction f_{esc} for the sources with a LyC detection. The large circle represents the LyC-LAEs subsample composite. Other symbols and curves represent literature measures and relations, respectively, as indicated by the legend. The correlation suggests that a prerequisite for a high f_{esc} is a large O32 value.

implied. Following Nakajima & Ouchi (2014), Izotov et al. (2016a, 2016b), and Nakajima et al. (2016), we can argue that LAEs and low- z LyC-confirmed green pea galaxies share the similarity in the line emission properties. This work can additionally deduce that both LyC-detected and non-detected LAEs share similar high [O III]/[O II] line ratios (see also Erb et al. 2016). Such large ratios, indicative of a high ionization parameter are not characteristic of continuum-selected sample at a similar redshift (Troncoso et al. 2014; Onodera et al. 2016; Sanders et al. 2016; Strom et al. 2017) as is confirmed by our own LBG subsample.

3.2. Ionizing Radiation Field

We finally consider the hardness of the ionizing radiation field, which is a further quantity related to the escaping radiation. The efficiency of ionizing photon production is conventionally parameterized by ξ_{ion} defined as:

$$\xi_{\text{ion},0} = \frac{Q_{\text{H}^0}}{L_{\text{UV}}}. \quad (1)$$

The number of ionizing photons, Q_{H^0} , can be determined via hydrogen recombination lines $\text{H}\beta$ (e.g., Leitherer & Heckman 1995), and the UV luminosity, L_{UV} , is derived from the Subaru photometry Paper I. The subscript 0 in $\xi_{\text{ion},0}$ indicates that the escape fraction of ionizing photons in this relation is assumed to be zero. The measurable quantity ξ_{ion} can then be derived by dividing $\xi_{\text{ion},0}$ by $(1 - f_{\text{esc}})$. Our pilot MOSFIRE program together with a rest-frame UV spectroscopic campaign conducted with VISible Multi-Object Spectrograph on the Very Large Telescope indicated that LAEs have ξ_{ion} values significantly larger than those for continuum-selected LBGs (Nakajima et al. 2016, 2018a; see also Matthee et al. 2017).

Figure 5 provides the distribution of ξ_{ion} for the various LACES subsamples. For the LyC-LAEs subsample we adopted an average escape fraction of $f_{\text{esc}} = 0.35$ to make the conversion. By improving the detectability of $\text{H}\beta$ through our recent MOSFIRE campaign, we can confirm our earlier suggestion that ξ_{ion} is significantly larger for LAEs than for continuum-selected LBGs. But again, we can see that both LyC-detected and non-detected LAEs subsamples have comparable values, $\log \xi_{\text{ion}} \simeq 25.5\text{--}25.7$, providing further evidence that the two populations of LAEs are spectroscopically indistinguishable. LAEs with LyC leakage are more efficient producers of ionizing photons at a given UV luminosity by $\simeq 0.3\text{--}0.4$ dex compared to continuum-selected LBGs but by only $\simeq 0.1$ dex with respect to our noLyC-LAEs. A similarly high ξ_{ion} is reported from another LyC leaker, *Ion3* (Vanzella et al. 2018).

4. Discussion

The original motivation for this series of papers was the view, following Nakajima & Ouchi (2014), that the unusually large O32 indices of LAEs (Figure 4) implied density-bound star-forming regions and thus a higher escape fraction of ionizing photons than for typical LBGs. In this sense, therefore, we considered the population as valuable analogs of sources in the reionization era for which direct measures of LyC leakage are currently not possible.

In this paper, we have shown in Figure 3 that a large O32 index is still a necessary condition for a significant f_{esc} , but that not all LAEs with large O32 values are LyC leakers. This implies that there may be a further additional physical property that must govern whether an LAE is a leaker. However, our examination of the full range of spectral diagnostics and the ionizing radiation field, respectively shown in Figures 2–5, reveals no fundamental distinction between LAE leakers and non-leakers. This follows a fundamental result we first introduced in Paper I of this series, namely the puzzling dichotomy of LyC detections in the overall LACES sample.

As metal-poor, compact star-forming systems, LAEs are likely being seen in an early phase of their evolution, providing abundant ionizing photons to explain their large O32 indices. This would result in physical conditions that allow LAEs to leak LyC photons more frequently than LBGs (Paper I; see also Steidel et al. 2018). A possible explanation for the dichotomy presented in Paper I further defined via the absence of any line diagnostic to separate leakers and non-leakers in the present analysis, is anisotropic leakage. In this hypothesis, the LACES sample would represent a fairly homogeneous sample, in terms of its spectroscopic properties and hardness of the radiation field, but the primary distinction between LyC-LAEs and noLyC-LAEs would be viewing angle. This could be considered as a less extreme version of the original density-bound nebula case discussed by Nakajima & Ouchi (2014) whereby the system is only partially porous to LyC radiation.

However, one important objection to a geometrical explanation is the fact that LyC leakers and non-leakers also have similar EW($\text{Ly}\alpha$) distributions (Paper I). If the paths of $\text{Ly}\alpha$ and LyC photons are similar, one might expect $\text{Ly}\alpha$ fluxes to be similarly diminished for the non-leakers. Indeed, leakages of both $\text{Ly}\alpha$ and LyC photons are indicated to be modulated by the covering fraction of the optically thick neutral gas (e.g., Reddy et al. 2016; Chisholm et al. 2018; Steidel et al. 2018). This point was discussed with the available $\text{Ly}\alpha$ data in

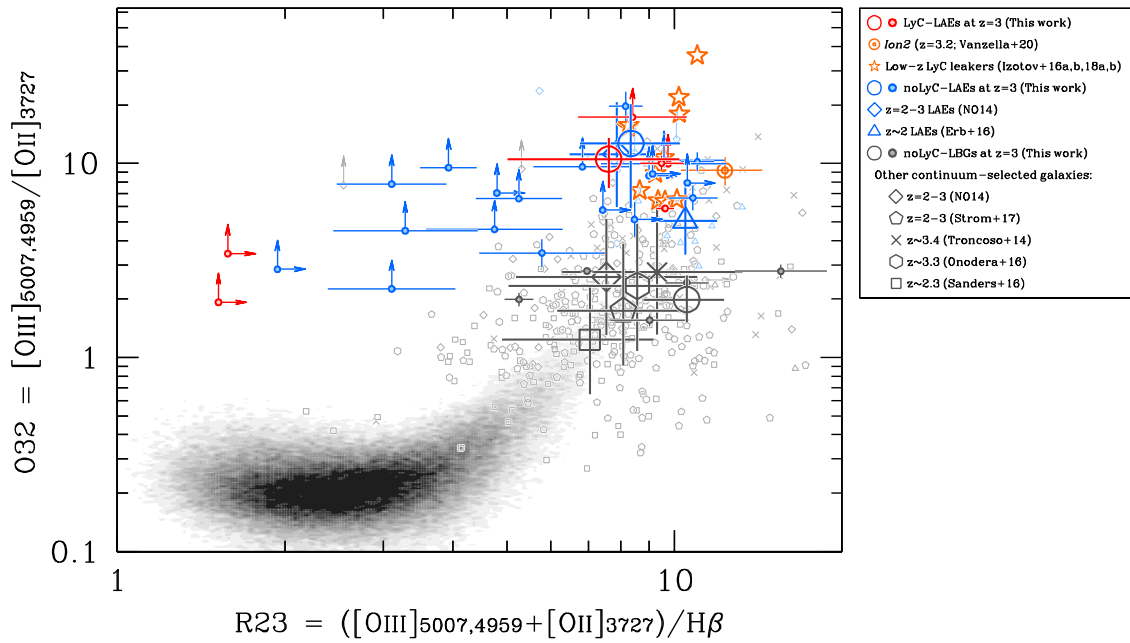


Figure 4. O32 vs. R23 diagram for the LACES and other samples. The LACES subsamples are shown with the same symbols and the colors as in Figure 2. Orange symbols show known LyC leakers, and blue and gray symbols show high- z LAEs and continuum-selected galaxies, respectively, compiled from the literature as shown by the legend. If O32 is provided without a [O III] λ 4959 contribution, we correct for it assuming the theoretical [O III] λ 5007/4959 line ratio of 2.98 (Storey & Zeppen 2000). Arrows provide 3σ lower limits. Gray shading illustrates the equivalent distribution for nearby SDSS galaxies.

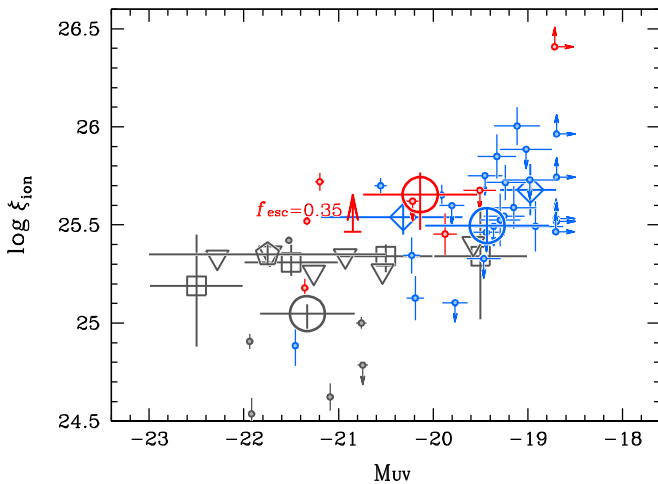


Figure 5. Ionizing photon production efficiency ξ_{ion} as a function of UV absolute magnitude. The symbols and colors for the LACES subsamples are as shown in Figure 2. Large symbols representing average ξ_{ion} values are derived from the stacked spectra (Section 2.3). The individual and the stacked ξ_{ion} are all dust-corrected as detailed in Section 2.4. The red upward arrow indicates the average degree of correction from $\xi_{\text{ion},0}$ to ξ_{ion} for the LyC-LAEs. Blue open diamonds present ξ_{ion} measurements for LAEs at $z=3$ (Nakajima et al. 2018a), and gray open symbols refer to ξ_{ion} measurements for continuum-selected galaxies at $z \sim 2-4$ (squares from Bouwens et al. 2016, inverse triangles from Shivaei et al. 2018, pentagon from Nakajima et al. 2018b).

Sections 5.1 and 6.1 of Paper I where correlations between f_{esc} and $\text{EW}(\text{Ly}\alpha)$ and its velocity were presented. By construction, all LACES targets must have prominent $\text{Ly}\alpha$ emission so sources with obscured $\text{Ly}\alpha$ will be absent, possibly weakening any expected trends.

While $\text{Ly}\alpha$ photons could preferentially escape along the same holes in the neutral medium as LyC photons, due to the resonant nature of the line, $\text{Ly}\alpha$ photons can also escape after

experiencing several scatterings. This would also explain why some LyC leakers present a higher escape fraction of $\text{Ly}\alpha$ photons than that of LyC photons (e.g., Verhamme et al. 2017). Moreover, the previous studies at high- z correlating the $\text{Ly}\alpha$ and LyC leakages with the covering fraction mostly investigate stacked LBGs with a weak $\text{Ly}\alpha$ emission (up to $\text{EW}(\text{Ly}\alpha) \sim 45 \text{ \AA}$), and hence in a low f_{esc} range (e.g., Reddy et al. 2016; Steidel et al. 2018). The correlation between $\text{Ly}\alpha$ and LyC found by stacking does not require that every LAE is necessarily a LyC emitter. For example, Japelj et al. (2017) investigate the LyC visibility of $z=3-4$ star-forming galaxies, most of which are LAEs, finding that none of them present significant emission of LyC radiation. Conversely, $\text{Ly}\alpha$ could be weakened from LyC emitters due to a spatial variation of neutral hydrogen column density across an object (e.g., *Ion1*; Vanzella et al. 2012; Ji et al. 2020; see also Erb et al. 2019 for suppression mechanisms of $\text{Ly}\alpha$ emission). Thus, while LyC leakage is broadly correlated with $\text{Ly}\alpha$ properties, it is unclear whether the tight correlation holds between the observed escape fractions of $\text{Ly}\alpha$ and LyC emission on an individual basis. Further data, e.g., higher resolution spectra sampling the $\text{Ly}\alpha$ emission line profile for our sources, would be advantageous to investigate these possibilities. If a narrow peak of $\text{Ly}\alpha$ emission is identified at systemic velocity, as seen in the other known LyC emitters of *Sunburst* (Rivera-Thorsen et al. 2017, 2019) and *Ion2* and *Ion3* (Vanzella et al. 2020), the detection of LyC emission would be attributed to a clear ionized channel along our line of sight.

Figure 6 shows the relationship between O32 and ξ_{ion} versus the EW of [O III] for the LACES sample, lower redshift extreme emission line galaxies (EELGs; Tang et al. 2019) and continuum-selected galaxies from the MOSDEF survey (Sanders et al. 2020). We can see that continuum-selected galaxies and less massive EELGs are similarly distributed in both panels. Since the $\text{EW}([\text{O III}])$ is an approximate measure of the age of the most recent star-formation activity (i.e., the

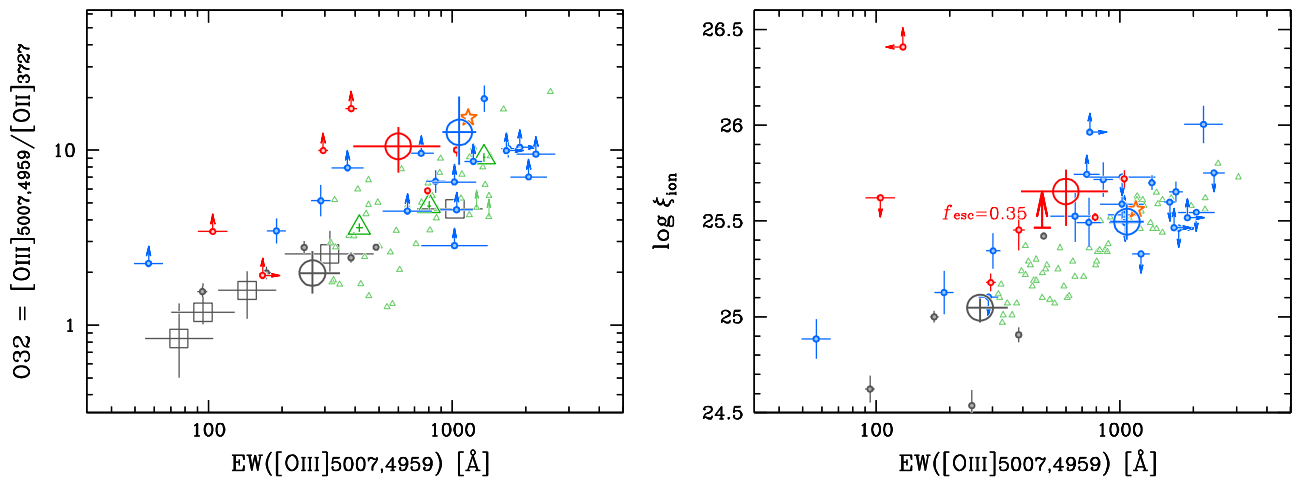


Figure 6. Relationship of [O III]/[O II] ratio (O32; left) and ionizing photon production efficiency (ξ_{ion} ; right) as a function of $EW([O III])$. The LACES sources are plotted with circles as shown in Figure 2. Green triangles present individual (small) and composite (large) measurements of extreme emission line galaxies (EELGs) at $z = 1.3\text{--}2.4$ (Tang et al. 2019). Orange star illustrates a low- z strong LyC emitting galaxy, J1154+2334, with $f_{esc} = 0.46$ (Izotov et al. 2018a; Schaerer et al. 2018). In the left panel, gray open squares show the O32 vs. $EW([O III])$ relationship derived with the composites of $z \sim 2.3$ continuum-selected galaxies from MOSDEF (Sanders et al. 2020). If O32 and/or $EW([O III])$ is provided without a [O III] $\lambda 4959$ contribution, we correct for it assuming the theoretical [O III] $\lambda 5007/4959$ line ratio of 2.98 (Storey & Zeippen 2000).

specific star-formation rate) as well as the ISM ionization and metallicity, the overall trends indicate younger stellar populations in a more highly ionized, lower metallicity environment have both a larger O32 and harder ξ_{ion} as shown by Tang et al. (2019).

However, despite these strong correlations, the LACES LAEs, both leakers and non-leakers, fall above the sequence, presenting an enhanced O32 for a given $EW([O III])$. Although different ISM conditions may partially explain the apparent difference in O32 between galaxies selected by Ly α and optical emission lines, such an enhancement in O32 would support some version of the density-bound or porous nebula hypothesis (Nakajima & Ouchi 2014). If the enhanced O32 is true and confirmed for both the leakers and non-leakers, the primary distinction between the two populations would be an independent physical property, such as viewing angle. Indeed, a local strong LyC leaking source, J1154+2443, with $f_{esc} = 0.46$ presents almost the same large values of O32, ξ_{ion} , and $EW([O III])$ as seen in the composite of noLyC-LAEs from our LACES sample (Schaerer et al. 2018), implying that noLyC-LAEs could have a condition to emit LyC radiation, but the pathway is not along our line of sight.

Admittedly, it is hard to verify the viewing angle explanation directly with the current data set. Conceivably examining Ly α profiles with higher spectral resolution than is currently available (e.g., Verhamme et al. 2015) and/or the depth of interstellar absorption lines in the rest-frame UV wavelength (e.g., Heckman et al. 2011; Reddy et al. 2016; Chisholm et al. 2018) might provide further evidence of the geometrical hypothesis. Interestingly, deep composite UV spectra of LAEs are reported to present a tantalizing trend that LAEs on average show shallow interstellar absorption lines, i.e., low covering fractions of low-ionization gas, significantly lower than those seen in LBGs (Jones et al. 2013; Trainor et al. 2015; Steidel et al. 2018), although it is not known which of these individual LAEs present a direct LyC leakage. Such an investigation for leakers and non-leakers over wider dynamic ranges of f_{esc} and $EW(Ly\alpha)$ would be useful to describe the origin of the f_{esc} -dichotomy and hence how ionizing photons escape from galaxies.

Finally, in Paper I we considered a spatial variation of the IGM transmission as a contributing factor to the leaker/non-leaker dichotomy noting the SSA22 field contains a proto-cluster at $z = 3.1$. Conceivably, the HI gas distribution may be complex (Mawatari et al. 2017; Hayashino et al. 2019). However, no spatial differences were seen between the distribution of LyC leakers and non-leakers in Paper I. We stress, however, that our current sample is too small for any significant clustering patterns to be discerned and so we still consider this explanation of the dichotomy discussed in this paper a plausible alternative. We plan to address this question via a LyC search from LAEs at lower redshifts where the IGM opacity and its variation is less important (Inoue et al. 2014).

In summary, we have extended our analysis of the spectroscopic properties of the LACES sample of $z \simeq 3.1$ LAEs from that presented in Paper I. Specifically, we have added measures of the O32 index (based on new Keck spectra sampling [O II] emission) as well as of ξ_{ion} , the hardness of the radiation field. Although a strong O32 index is a necessary condition for escaping radiation, we find that both LyC leakers and non-leakers have similar O32 and ξ_{ion} values, suggesting that an additional physical property must govern whether escaping radiation can be detected with *HST*. Our results support the hypothesis that most LACES LAEs are likely emitting LyC radiation through a porous interstellar medium but suggest that only a fraction are being viewed favorably by the observer as LyC leakers.


The W. M. Keck observations were carried out within the framework of Subaru-Keck time exchange program, where the travel expense was supported by the Subaru Telescope, which is operated by the National Astronomical Observatory of Japan. Some of the data presented herein were obtained at the W. M. Keck Observatory, which is operated as a scientific partnership among the California Institute of Technology, the University of California and the National Aeronautics and Space Administration. The Observatory was made possible by the generous financial support of the W. M. Keck Foundation. The authors wish to recognize and acknowledge the very significant cultural role and reverence that the summit of Maunakea has always

had within the indigenous Hawaiian community. We are most fortunate to have the opportunity to conduct observations from this mountain. We thank the anonymous referee for helpful comments and discussions that improved our manuscript. R.S.E. acknowledges funding from the European Research Council (ERC) under the European Union's Horizon 2020 research and innovation programme (grant agreement No. 669253). B.E.R. acknowledges support from NASA program *HST-GO-14747*, contract NNG16PJ25C, and grant 17-ATP17-0034. The Cosmic DAWN Center is funded by the Danish National Research Foundation.

Facility: Keck I (MOSFIRE).

ORCID iDs

Kimihiko Nakajima  <https://orcid.org/0000-0003-2965-5070>

Richard S. Ellis  <https://orcid.org/0000-0001-7782-7071>

Brant E. Robertson  <https://orcid.org/0000-0002-4271-0364>

References

- Behrens, C., Dijkstra, M., & Niemeyer, J. C. 2014, *A&A*, 563, A77
- Bouwens, R. J., Illingworth, G. D., Oesch, P. A., et al. 2015, *ApJ*, 811, 140
- Bouwens, R. J., Smit, R., Labbé, I., et al. 2016, *ApJ*, 831, 176
- Chisholm, J., Gazagnes, S., Schaerer, D., et al. 2018, *A&A*, 616, A30
- Dayal, P., & Ferrara, A. 2018, *PhR*, 780, 1
- de Barros, S., Vanzella, E., Amorín, R., et al. 2016, *A&A*, 585, A51
- Erb, D. K., Berg, D. A., Auger, M. W., et al. 2019, *ApJ*, 884, 7
- Erb, D. K., Pettini, M., Steidel, C. C., et al. 2016, *ApJ*, 830, 52
- Faisst, A. L. 2016, *ApJ*, 829, 99
- Fletcher, T. J., Tang, M., Robertson, B. E., et al. 2019, *ApJ*, 878, 87
- Gordon, K. D., Clayton, G. C., Misselt, K. A., Landolt, A. U., & Wolff, M. J. 2003, *ApJ*, 594, 279
- Hayashino, T., Inoue, A. K., Kousai, K., et al. 2019, *MNRAS*, 484, 5868
- Hayashino, T., Matsuda, Y., Tamura, H., et al. 2004, *AJ*, 128, 2073
- Heckman, T. M., Borthakur, S., Overzier, R., et al. 2011, *ApJ*, 730, 5
- Inoue, A. K., Shimizu, I., Iwata, I., & Tanaka, M. 2014, *MNRAS*, 442, 1805
- Izotov, Y. I., Orlitová, I., Schaerer, D., et al. 2016a, *Natur*, 529, 178
- Izotov, Y. I., Schaerer, D., Thuan, T. X., et al. 2016b, *MNRAS*, 461, 3683
- Izotov, Y. I., Schaerer, D., Worseck, G., et al. 2018a, *MNRAS*, 474, 4514
- Izotov, Y. I., Worseck, G., Schaerer, D., et al. 2018b, *MNRAS*, 478, 4851
- Japelj, J., Vanzella, E., Fontanot, F., et al. 2017, *MNRAS*, 468, 389
- Jaskot, A. E., Dowd, T., Oey, M. S., Scarlata, C., & McKinney, J. 2019, *ApJ*, 885, 96
- Jaskot, A. E., & Oey, M. S. 2013, *ApJ*, 766, 91
- Ji, Z., Giavalisco, M., Vanzella, E., et al. 2020, *ApJ*, 888, 109
- Jones, T. A., Ellis, R. S., Schenker, M. A., & Stark, D. P. 2013, *ApJ*, 779, 52
- Kewley, L. J., & Dopita, M. A. 2002, *ApJS*, 142, 35
- Leitherer, C., & Heckman, T. M. 1995, *ApJS*, 96, 9
- Maiolino, R., Nagao, T., Grazian, A., et al. 2008, *A&A*, 488, 463
- Marchi, F., Pentericci, L., Guaita, L., et al. 2017, *A&A*, 601, A73
- Marchi, F., Pentericci, L., Guaita, L., et al. 2018, *A&A*, 614, A11
- Matsuda, Y., Yamada, T., Hayashino, T., et al. 2005, *ApJL*, 634, L125
- Matthee, J., Sobral, D., Best, P., et al. 2017, *MNRAS*, 465, 3637
- Mawatari, K., Inoue, A. K., Yamada, T., et al. 2017, *MNRAS*, 467, 3951
- Naidu, R. P., Forrest, B., Oesch, P. A., Tran, K.-V. H., & Holden, B. P. 2018, *MNRAS*, 478, 791
- Nakajima, K., Ellis, R. S., Iwata, I., et al. 2016, *ApJL*, 831, L9
- Nakajima, K., Fletcher, T., Ellis, R. S., Robertson, B. E., & Iwata, I. 2018a, *MNRAS*, 477, 2098
- Nakajima, K., & Ouchi, M. 2014, *MNRAS*, 442, 900
- Nakajima, K., Schaerer, D., Le Fèvre, O., et al. 2018b, *A&A*, 612, A94
- Onodera, M., Carollo, C. M., Lilly, S., et al. 2016, *ApJ*, 822, 42
- Reddy, N. A., Kriek, M., Shapley, A. E., et al. 2015, *ApJ*, 806, 259
- Reddy, N. A., Shapley, A. E., Sanders, R. L., et al. 2018, *ApJ*, 869, 92
- Reddy, N. A., Steidel, C. C., Pettini, M., Bogosavljević, M., & Shapley, A. E. 2016, *ApJ*, 828, 108
- Rivera-Thorsen, T. E., Dahle, H., Chisholm, J., et al. 2019, *Sci*, 366, 738
- Rivera-Thorsen, T. E., Dahle, H., Gronke, M., et al. 2017, *A&A*, 608, L4
- Roberts-Borsani, G. W., Bouwens, R. J., Oesch, P. A., et al. 2016, *ApJ*, 823, 143
- Robertson, B. E., Ellis, R. S., Furlanetto, S. R., & Dunlop, J. S. 2015, *ApJL*, 802, L19
- Robertson, B. E., Furlanetto, S. R., Schneider, E., et al. 2013, *ApJ*, 768, 71
- Rutkowski, M. J., Scarlata, C., Henry, A., et al. 2017, *ApJL*, 841, L27
- Sanders, R. L., Shapley, A. E., Kriek, M., et al. 2016, *ApJ*, 816, 23
- Sanders, R. L., Shapley, A. E., Reddy, N. A., et al. 2020, *MNRAS*, 491, 1427
- Schaerer, D., Izotov, Y. I., Nakajima, K., et al. 2018, *A&A*, 616, L14
- Shapley, A. E., Reddy, N. A., Kriek, M., et al. 2015, *ApJ*, 801, 88
- Shapley, A. E., Steidel, C. C., Strom, A. L., et al. 2016, *ApJL*, 826, L24
- Shivaei, I., Reddy, N. A., Siana, B., et al. 2018, *ApJ*, 855, 42
- Siana, B., Shapley, A. E., Kulas, K. R., et al. 2015, *ApJ*, 804, 17
- Smit, R., Bouwens, R. J., Franx, M., et al. 2015, *ApJ*, 801, 122
- Stark, D. P. 2016, *ARA&A*, 54, 761
- Steidel, C. C., Bogosavljević, M., Shapley, A. E., et al. 2018, *ApJ*, 869, 123
- Storey, P. J., & Zeppen, C. J. 2000, *MNRAS*, 312, 813
- Strom, A. L., Steidel, C. C., Rudie, G. C., et al. 2017, *ApJ*, 836, 164
- Tang, M., Stark, D. P., Chevallard, J., & Charlot, S. 2019, *MNRAS*, 489, 2572
- Trainor, R. F., Steidel, C. C., Strom, A. L., & Rudie, G. C. 2015, *ApJ*, 809, 89
- Trainor, R. F., Strom, A. L., Steidel, C. C., & Rudie, G. C. 2016, *ApJ*, 832, 171
- Troncoso, P., Maiolino, R., Sommariva, V., et al. 2014, *A&A*, 563, A58
- Vanzella, E., Caminha, G. B., Calura, F., et al. 2020, *MNRAS*, 491, 1093
- Vanzella, E., de Barros, S., Castellano, M., et al. 2015, *A&A*, 576, A116
- Vanzella, E., de Barros, S., Vasei, K., et al. 2016, *ApJ*, 825, 41
- Vanzella, E., Guo, Y., Giavalisco, M., et al. 2012, *ApJ*, 751, 70
- Vanzella, E., Nonino, M., Cupani, G., et al. 2018, *MNRAS*, 476, L15
- Verhamme, A., Orlitová, I., Schaerer, D., et al. 2017, *A&A*, 597, A13
- Verhamme, A., Orlitová, I., Schaerer, D., & Hayes, M. 2015, *A&A*, 578, A7
- Yamada, T., Nakamura, Y., Matsuda, Y., et al. 2012, *AJ*, 143, 79
- Zackrisson, E., Inoue, A. K., & Jensen, H. 2013, *ApJ*, 777, 39